MNRAS **000**, 1–16 (2019) Preprint 15 October 2019 Compiled using MNRAS LaTeX style file v3.0

The effect of gas accretion on the radial gas metallicity profile of simulated galaxies

Florencia Collacchioni,[1,2]⋆ Claudia D. P. Lagos,[3,4,5] Peter D. Mitchell,[6,7] Joop Schaye,[6,] Emily Wisnioski,[4,8] Sofía A. Cora,[1,2] and Camila A. Correa[6]
[1]*Instituto de Astrofísica de La Plata (CCT La Plata, CONICET,UNLP), Observatorio Astronómico, Paseo del Bosque, B1900FWA, La Plata, Argentina.*
[2]*Facultad de Ciencias Astronómicas y Geofísicas, Universidad Nacional de La Plata, Observatorio Astronómico, Paseo del Bosque, B1900FWA La Plata, Argentina.*
[3]*International Centre for Radio Astronomy Research (ICRAR), M468, University of Western Australia, 35 Stirling Hwy, Crawley, WA 6009, Australia.*
[4]*Australian Research Council Centre of Excellence for All Sky Astrophysics in 3 Dimensions (ASTRO 3D).*
[5]*Cosmic Dawn Center (DAWN), Niels Bohr Institute, University of Copenhagen/DTU-Space, Technical University of Denmark, Nørregade 10, 1165 København, Denmark.*
[6]*Leiden Observatory, Leiden University, P.O. Box 9513, NL-2300 RA Leiden, The Netherlands.*
[7]*Université Lyon, Université Lyon1, Ens de Lyon, CNRS, Centre de Recherche Astrophysique de Lyon UMR5574, F-69230, Saint-Genis-Laval, France.*
[8]*Research School of Astronomy and Astrophysics, Australian National University, Canberra, ACT 2611, Australia.*

Accepted XXX. Received YYY; in original form ZZZ

ABSTRACT
We study the effect of the gas accretion rate ($\dot{M}_{\rm accr}$) on the radial gas metallicity profile (RMP) of galaxies using the EAGLE cosmological hydrodynamic simulations, focusing on central galaxies of stellar mass $M_\star \gtrsim 10^9$ M$_\odot$ at $z \leq 1$. We find clear relations between $\dot{M}_{\rm accr}$ and the slope of the RMP (measured within an effective radius), where higher $\dot{M}_{\rm accr}$ are associated with more negative slopes. The slope of the RMPs depends more strongly on $\dot{M}_{\rm accr}$ than on stellar mass, star formation rate or gas fraction, suggesting $\dot{M}_{\rm accr}$ to be a more fundamental driver of the RMP slope of galaxies. We find that eliminating the dependence on stellar mass is essential for pinning down the properties that shape the slope of the RMP. Although $\dot{M}_{\rm accr}$ is the main property modulating the slope of the RMP, we find that it causes other correlations that are more easily testable observationally: at fixed stellar mass, galaxies with more negative RMP slopes tend to have higher gas fractions and SFRs, while galaxies with lower gas fractions and SFRs tend to have flatter metallicity profiles within an effective radius.

Key words: methods: numerical – galaxies: evolution – galaxies: formation

1 INTRODUCTION

The mass–metallicity relation (MZR) is the correlation between the gas-phase metallicity of galaxies and their stellar mass and has been established both in observations (e.g. Tremonti et al. 2004; Maiolino et al. 2008; Troncoso et al. 2014) and galaxy formation simulations (e.g. De Rossi et al. 2015, 2017; Ma et al. 2016; Collacchioni et al. 2018; Tissera et al. 2019) throughout a wide range in look-back time, 0 to ≈ 12 Gyr. The chemical enrichment of galaxies is expected to be the result of the interplay between inflows of pristine gas, outflows of enriched material and the star formation history of galaxies (Finlator & Davé 2008; Zahid et al. 2014; Bothwell et al. 2016), and hence the study of the MZR holds important information about the formation of galaxies.

In the last decade, integral field spectroscopy (IFS) data such as CALIFA (Sánchez et al. 2012), KMOS (Stott et al. 2014), SAMI (Bryant et al. 2015; Poetrodjojo et al. 2018) and MUSE (Carton et al. 2018; Erroz-Ferrer et al. 2019) have greatly expanded the study of the MZR by providing spatially resolved information of the abundance of metals in galaxies, opening a new window onto the importance of chemical enrichment in the evolution of galaxies.

The study of radial metallicity profiles (RMP), i.e., the abundance of metals locked in the gas component of galaxies, typically measured through nebular emission lines (see Maiolino & Mannucci 2019 for a recent review), as a function of the distance to the centre of their galaxy, can help to

⋆ E-mail:fcollacchioni@fcaglp.unlp.edu.ar

understand how chemical enrichment takes place in galaxies. This is usually quantified as $\log_{10}(Z_{\rm gas}/Z_{\odot}) = \alpha\, r + b$, with $Z_{\rm gas}/Z_{\odot}$ being the gas metallicity in units of solar metallicity, and α being the slope of the RMP. Pioneering studies found that low-redshift galaxies ($z \leq 0.5$) display a negative RMP gradient ($\alpha < 0$), i.e., galaxies are more chemically enriched in the central regions than in the outskirts (Sánchez et al. 2012, 2013; Ho et al. 2015). This is generally interpreted through the inside-out formation scenario, in which stars at the centre of galaxies form earlier than those in the outskirts and hence have had more time to enrich the interstellar medium (ISM), naturally producing higher gas metallicities in the centre compared to the outskirts (Boissier & Prantzos 1999). However, further studies have found a variety of RMPs that complicates the picture. For example, Troncoso et al. (2014), based on the AMAZE project, found that $3 \lesssim z \lesssim 4$ galaxies display *positive* RMPs ($\alpha > 0$), which the authors interpret as low-metallicity gas flowing directly into the centres of galaxies (see also Cresci et al. 2010).

Instead of measuring a single α for the whole RMP, Sánchez et al. (2014) and Sánchez-Menguiano et al. (2016) using the CALIFA survey, and Belfiore et al. (2017) using the SSDS-IV MaNGA survey (among others authors), fit the RMP with two power laws, i.e. two different α for the inner and outer regions, finding puzzling results that cannot be easily interpreted within the inside-out scenario, such as a flattening in the outer regions, $\alpha \approx 0$, or relatively flat inner profiles (at least, less negative than expected) in high-mass galaxies ($M_{\star} \gtrsim 10^{10}\,{\rm M}_{\odot}$, Sánchez-Menguiano et al. 2016). This could be linked to feedback removing metals preferentially from the inner regions of the galaxy (e.g. Lagos et al. 2013; Muratov et al. 2017), as well as significant star formation (SF) in the outer regions of the galaxy (for example, due to mergers or close interactions) that can quickly enrich the gas.

Several studies have explored the possible physical causes behind the shape of the RMP. According to Sánchez et al. (2012), the change in the outer regions (beyond ≈ 2 times the effective radius) could be due to different gas densities, the SF history, or even the presence of bars which can alter the flow of gas internal to galaxies. Yet, Zinchenko et al. (2019), also using the CALIFA survey, found no correlation between the RMP gradient and bars or spiral patterns, and Carton et al. (2018) did not find a correlation between α and the SF rate (SFR) or stellar masses of galaxies when analysing MUSE data. This is in tension with the reports of weak correlations between α and the specific SFR (sSFR = SFR/$M_{\star}$) by Stott et al. (2014) and Wuyts et al. (2016) using KMOS surveys, and with stellar mass by Ho et al. (2015) who use a combined CALIFA and SDSS Data Release 7 galaxy sample. Moreover, Ho et al. (2015) found that measuring the RMP normalised by the galaxy's effective radius does lead to a correlation between α and galaxy properties, implying a co-evolution of gas and stars.

It is fair to say that there is tension between the different observational results, which may in part be due to the different selection of galaxies, but also perhaps suggesting that the RMP is not well described by a single or double power-law, and/or that other galaxy properties may do correlate more strongly with the RMP than sSFR, stellar mass and morphology. In fact, Carton et al. (2015), measuring atomic hydrogen gas content (HI) with the WSRT of 50 SDSS galaxies, found that the RMP slopes show a strong correlation with the HI mass fraction (the HI-to-stellar mass ratio), such that galaxies with higher HI mass fractions also have more negative α.

From a theoretical perspective, a range of results from hydrodynamical simulations of galaxy formation have been reported that do not necessarily agree with each other. Tissera et al. (2016), using a simulated cubic volume of 14 Mpc of side, argued that very negative α can be achieved through close encounters, presence of bars and/or low-metallicity gas accretion in the central regions of galaxies, while Sillero et al. (2017) concluded that galaxy interactions lead to $\alpha > 0$ when analysing simulated disc galaxies. Recently, using the reference EAGLE simulation (Schaye et al. 2015; Crain et al. 2015), Tissera et al. (2019) showed that very active merger histories are associated with galaxies displaying flatter RMPs. Tissera et al. (2016) and Sillero et al. (2017) agree in that galaxies with stellar masses $M_{\star} \leq 10^{10}\ {\rm M}_{\odot}$ show more negative RMPs than more massive ones, but Ma et al. (2017), using cosmological zoom-in simulations from the FIRE project (Hopkins et al. 2014), report low-mass galaxies to have flatter RMPs compared to massive galaxies. Tissera et al. (2019) also found no correlation between α and the environment in which galaxies live, while the physical size of the gaseous disc of galaxies appeared as one of the only galaxy properties clearly correlated with α, in a way that more extended gas discs are associated with more negative α. Interestingly, Tissera et al. (2016) find that as redshift increases, high-mass galaxies ($M_{\star} \geq 10^{10}\ {\rm M}_{\odot}$) show less negative and sometimes even positive α.

Gas accretion is expected to shape both the SF and metallicity histories of galaxies and, hence, one would like to explore directly the correlation between the RMP and the gas accretion rate ($\dot{M}_{\rm accr}$). However, $\dot{M}_{\rm accr}$ is not easily accessible in observations, motivating the simulation-based work to explore indirect tracers, such as SF and stellar mass. SF is expected to be proportional to the gas supply, such that more infalling gas can trigger more star formation (e.g. Davé et al. 2011), while more massive galaxies live in more massive halos (Behroozi et al. 2013) and hence should be able to attract more gas into their gravitational potential. By studying directly the effect of gas supply onto galaxies, Perez et al. (2011) found that more negative slopes are associated with low-metallicity gas accretion, while Sillero et al. (2017) predicted a correlation between α and sSFR only in cases where the gas inflow triggers SF within the central regions on short timescales. The proposed scenario is that significant $\dot{M}_{\rm accr}$ onto the central regions of galaxies can increase the gas density, triggering high levels of SF which rapidly enrich the inner regions of galaxies, leading to more negative slopes of the RMP. Other studies suggest extreme accretion, i.e. mergers, yields inverted metallicity gradients (Troncoso et al. 2014). Hence, the study of RMPs might be essential to constrain the properties of the gas that is being accreted onto the galaxies (i.e. pristine or pre-enriched), and the effect $\dot{M}_{\rm accr}$ has on their chemical evolution (Finlator 2017).

The main limitation of the above studies is that they tend to focus on a small number of simulated galaxies, and hence it is difficult to separate effects related to gas accretion from other physical effects, such as galaxy mergers/interactions, depth of the gravitational potential well, and gas outflows. It is therefore essential to explore theoretically how $\dot{M}_{\rm accr}$ affects the RMP of galaxies across cosmic time in a large sample of simulated galaxies over cosmologically representative volumes. This is the context in which our work develops. We use the EAGLE cosmological hydrodynamical simulations suite to study how $\dot{M}_{\rm accr}$ correlates with the RMPs, breaking the RMP into different regions of the galaxies. Our objective is to understand which regions of galaxies are most affected by the gas supply, what the roles of stellar mass, SFR and gas content are in determining the RMP, and what the "smoking guns" of gas accretion are that can be seen in the RMP. We do this by combining simulated boxes at different resolutions to allow us to cover the stellar mass range $M_\star > 10^9\,{\rm M}_\odot$ at $0 \le z \le 1$.

This paper is organised as follows. In Section 2, we briefly summarise the cosmological hydrodynamic simulations used in this work, as well as the galaxy sample selected, and introduce our definition of $\dot{M}_{\rm accr}$. We analyse how the RMP changes with $\dot{M}_{\rm accr}$, stellar mass, SFR and gas content in Section 3, and show that $\dot{M}_{\rm accr}$ is the property that is most strongly correlated with the slope of the RMP. In Section 4, we discuss the scope of our results and limitations, as well as the possibility of measuring the correlations found here in observations. Finally, our conclusions are presented in Section 5.

2 EAGLE SIMULATIONS

The EAGLE project[1] is a set of cosmological hydrodynamical simulations that differ in box size, number of particles, numerical resolution and subgrid physics. A brief description of the simulations and the underlying subgrid models is presented in this section. For more information on the model, the reader can refer to Schaye et al. (2015, hereafter S15) and Crain et al. (2015), while the public data release is documented in McAlpine et al. (2016). To run the EAGLE simulations, a modification of the N-body Tree-PM smoothed particle hydrodynamics (SPH) code GADGET-3 (last described by Springel 2005) is used, with the numerical methods referred to as ANARCHY (Schaller et al. 2015).

EAGLE follows the evolution of dark matter and gas particles, consistent with a flat ΛCDM cosmology characterised by the Planck Collaboration et al. (2014) parameters: matter density $\Omega_{\rm m} = 0.307$, dark energy density $\Omega_\Lambda = 0.693$, baryon matter density $\Omega_{\rm b} = 0.04825$, square root of linear variance of matter distribution $\sigma_8 = 0.8288$, index of power spectrum of primordial adiabatic perturbations $n_{\rm s} = 0.9611$, Hubble parameter $H_0 = 100\,h^{-1}\,{\rm km\,s^{-1}\,Mpc^{-1}}$ with $h = 0.6777$, and primordial helium abundance $Y = 0.248$.

A Friend-of-Friends (FOF; Davis et al. 1985) algorithm is used to identify haloes of dark matter (DM) particles; while the SUBFIND algorithm (Springel et al. 2001; Dolag et al. 2009) is used to identify the gravitationally bound subhaloes within a FOF structure, linking the gas particles with their nearest DM particles. Theses subhaloes are then defined as the galaxies in the simulation. For each FOF halo, the subhalo that contains the particle with the lowest gravitational potential value is defined as a central, and satellite galaxies are all of the remaining subhaloes.

The subgrid physical models implemented in the EAGLE simulations are the following. Radiative cooling and photoheating on 11 elements (H, He, C, N, O, Ne, Mg, Si, S, Ca and Fe) are applied (Wiersma et al. 2009a), accounting not only for variations in metallicity but also in relative abundances. Hydrogen reionization is implemented as described in S15 at $z = 11.55$. Star formation follows the description in Schaye & Dalla Vecchia (2008), with a metallicity-dependent density threshold, in order to have a more realistic description of the gas transitions between warm, neutral and cold phases (Schaye 2004). A Chabrier stellar mass function (IMF, Chabrier 2003) is adapted, with minimum and maximum masses of 0.1 and 100 ${\rm M}_\odot$, respectively. Stellar mass loss (Wiersma et al. 2009b), and mass and energy losses from Type II and Ia supernovae (SNe) are also implemented. Energy from SN is stochastically injected in nearby gas particles in the form of thermal feedback as in Dalla Vecchia & Schaye (2012). In a similar way, feedback from active galactic nuclei (AGN) is computed with a fixed efficiency, and the energy is injected into the surrounding gas medium in a thermally and stochastic way (for details see S15).

The simulations have been calibrated with the observed $z \approx 0$ galaxy stellar mass function (GSMF), the relation between the galaxy stellar and black hole (BH) mass, and galaxy sizes of star forming galaxies. For this work, we use two of the EAGLE simulations: the recalibrated high-resolution simulation of a 25^3 cMpc^3 volume, which we will refer to as Recal-L25N752, and the reference simulation of a 100^3 cMpc^3 volume, called Ref-L100N1504. DM particle masses are 1.21×10^6 ${\rm M}_\odot$ for the former and 9.7×10^6 ${\rm M}_\odot$ for the latter, while the gas particle masses are 2.26×10^5 ${\rm M}_\odot$ and 1.81×10^6 ${\rm M}_\odot$, respectively.

Several papers have shown that the reference EAGLE simulation reproduces many observed properties of galaxies relatively well, such as the stellar mass function evolution from $z = 0$ to $z = 4$, the main sequence of galaxies (Furlong et al. 2015), the colour distribution of galaxies (Trayford et al. 2015; Wright et al. 2019), and the gas content of galaxies of a given stellar mass (Lagos et al. 2015, 2016; Bahé et al. 2016; Crain et al. 2017). Very relevant for this work, the mass-metallicity relation of stars and gas, the resolved mass-metallicity relation (Trayford & Schaye 2019), as well as the gas metallicity gradients (S15, Tissera et al. 2019), are well reproduced at $M_\star \gtrsim 10^{10}$ ${\rm M}_\odot$ for Ref-L100N1504. At lower stellar masses, deviations from the observations become important. The higher resolution, recalibrated run of the EAGLE suite alleviates this problem, enabling agreement down to stellar masses of 10^9 ${\rm M}_\odot$ (see S15, De Rossi et al. 2017). Hence, the simultaneous use of both the Ref-L100N1504 and the Recal-L25N752 simulations allows us to have very good statistics above 10^{10} ${\rm M}_\odot$ in stellar mass (mostly from the Ref-L100N1504 simulation), and to push down to 10^9 ${\rm M}_\odot$, thanks to the Recal-L25N752 simulation, with confidence that the observed mass-metallicity relation is well reproduced over the entire stellar mass range. However, we keep the analysis of the two simulated samples separated, unless otherwise stated. We remind the reader that the Recal-L25N752 simulation has slightly different parameters for the stellar and AGN feedback, as the aim of that

[1] http://icc.dur.ac.uk/Eagle/

run was to reproduce the $z = 0.1$ stellar mass function with a higher resolution (see discussion on weak and strong convergence in S15).

2.1 Computation of the gas accretion rate

We compute $\dot{M}_{\rm accr}$ onto galaxies using a simple particle tracking methodology (following Neistein et al. 2012). For a given subhalo at a given simulation snapshot, we first identify gas particles that are classified as star forming (SF), as described in S15. We then define accreting gas particles as the subset of these that are:
(a) bound to the main progenitor subhalo at the previous (earlier) snapshot in the merger tree, and
(b) not star forming at that time.
Star particles that fulfil conditions *(a)* and *(b)* are also taken into account in the calculation of the accreting gas. These stellar particles are those that come from gas particles that were accreted as of the previous snapshot. With this criteria, we ensure the accreting gas came from the same subhalo studied and, at the same time, that the accretion itself changes the state of the gas (from non-SF to SF). In other words, we are interested in inflows that can trigger SF. The latter is done to more easily connect with the observations, in which nebular emission lines are used as gas tracers and to measure the gas metallicity.

The choice of only counting the gas coming from the main progenitor is to compute the contribution of the accreted gas that comes from the diffuse circumgalactic medium (CGM) rather than galaxy mergers. We remark that previous hydrodynamical simulations show this "smooth accretion" to be the main source of gas accretion onto galaxies (van de Voort et al. 2011). Wright et al. in preparation show that in EAGLE 80% or more of the gas accreted onto halos comes from smooth accretion (which includes both pristine accretion and pre-processed gas). $\dot{M}_{\rm accr}$ is then simply defined as the mass of accreted gas particles that satisfy conditions *(a)* and *(b)*, divided by the time interval between the snapshots. Progenitor subhaloes are identified using merger trees generated with the DHalo algorithm (Jiang et al. 2014; Qu et al. 2017).

For the Ref-L100N1504 simulation, we use 50 snapshots to compute $\dot{M}_{\rm accr}$, while for Recal-L25N752 we use 29 snapshots. The reason why we use different numbers of snapshots, is that for Ref-L100N1504 we have available a larger number of outputs with a better time cadence but with a reduced number of gas particle properties, also called "snipshots", compared to the default 29 snapshots that are publicly available from the EAGLE database (McAlpine et al. 2017). For Recal-L25N752, however, we use the public data, which includes 29 snapshots, with the complete list of particle properties. The time interval between outputs for Ref-L100N1504 is 0.42 Gyr from $z = 0 \rightarrow 0.03$, and 0.4 Gyr from $z = 1 \rightarrow 1.05$, while for Recal-L25N752 the time interval between outputs is 1.34 Gyr from $z = 0 \rightarrow 0.1$, and 0.93 Gyr from $z = 1 \rightarrow 1.26$. Although we are using different timesteps to compute accretion rates in the two simulations, this does not have an important impact on our results as accretion happens in long timescales (see Mitchell et al. in prep. and Wright et al. in prep.). If we were studying outflows, however, this difference in time cadence would be important, as outflows happen in short timescales and are most stochastic. Hereafter, we use the word "snapshots" to refer to both these sets of outputs, making it clear which simulations we are referring to.

There is, however, an inherent weakness of the particle tracking method. If there is inflow that joins the SF ISM but leaves it before the snapshot in which the accreted gas is identified (with "leave" we mean that the particles are transferred to another phase, e.g. NON-SF ISM), then that inflow will not be counted. For more details about the method implemented here to measure the accreted gas, the reader can refer to Mitchell et al. (in preparation).

2.2 Simulated galaxy sample

Because of how sensitive the infalling gas is to environmental effects such as tidal stripping, ram pressure stripping, interactions, etc., which predominantly affect satellite galaxies, we limit this study to central, star-forming galaxies only (i.e. the galaxy sitting in the deepest part of the potential well of halos). We also apply the restriction of using only galaxies with $M_\star \geq 10^9$ $M_\odot$ for the Recal-L25N752 simulation and $M_\star \geq 10^{10}$ $M_\odot$ for the Ref-L100N1504 one, due to the resolution of the respective simulations (which gives us a minimum star particles number of ≈ 6700 and ≈ 7700, respectively). We include those central galaxies whose $\dot{M}_{\rm accr}$ corresponds to at least 10 SF gas particles, which translates to $\dot{M}_{\rm accr} \approx 9\times10^{-2}$ $M_\odot$ yr^{-1} at $z = 0$ and $\dot{M}_{\rm accr} \approx 5\times10^{-2}$ $M_\odot$ yr^{-1} at $z = 1$. In Appendix A, we test our main results against different choices of the latter minimum number of SF particles, and found them to be insensitive to thresholds up to 100 particles. Our results are therefore well converged against this limit.

Our final sample comprises a total of 1,280 galaxies at $z = 0$ and 1,642 at $z = 1$. Because of the size evolution of galaxies (galaxies at higher redshift are smaller at fixed stellar mass Furlong et al. 2017), we limit our study to $z \leq 1$, for which galaxies are better resolved. The median physical sizes of our selected galaxies[2] in the Recal-L25N752 simulation are 3.98 kpc and 3.17 kpc at redshifts $z = 0$ and 1, respectively. Similarly, the median galaxy sizes of our selected sample in the Ref-L100N1504 simulation are 4.22 kpc and 3.11 kpc at redshifts $z = 0$ and 1, respectively. Recall that the latter galaxies are more massive than the ones selected from the Recal-L25N752 simulation. In both cases, these sizes are comfortably above the gravitational softening of the corresponding simulation, which are 0.35 proper kpc and 0.70 proper kpc for Recal-L25N752 and Ref-L100N1504, respectively. Ludlow et al. (2019) showed that the spatial resolution of a simulation is approximately 0.05 times the mean particle spacing, which for the Ref-L100N1504 and Recal-L25N752 are 66.5 physical kpc and 33.35 physical kpc at $z = 0$, respectively, leading to a spatial resolution of 3.3 kpc and 1.6 kpc, respectively. This shows that the stellar mass selection applied here selects well resolved galaxies in these two simulations.

[2] We compute the median value and dispersion of the half-stellar mass radius, r_{50}, for the whole sample at each redshift and simulation.

2.3 Estimation of the gas metallicity profile

Since we are interested in studying how the gas metallicity profiles are altered by $\dot{M}_{\rm accr}$, we need to define the way in which this profile is measured. Unless otherwise stated, we consider SF gas particles in spherical shells that increase in physical bins of 1 kpc from 1 to 9 kpc, followed by bins of 3 kpc width up to 51 kpc, by bins of 10 kpc until 101 kpc, and by bins of 50 kpc width up to 501 kpc. This is done to avoid shot noise caused by the density of SF particles decreasing steeply with radius. The metallicity of the gas contained within each shell is defined as the ratio between the mass in metals heavier than helium over the total mass of gas, that is

$$Z = \frac{M_{\rm metals}}{M_{\rm H} + M_{\rm He} + M_{\rm metals}}, \quad (1)$$

where $M_{\rm H}$, $M_{\rm He}$ and $M_{\rm metals}$ are the masses of hydrogen, helium and metals of the SF gas particles, respectively. We use a logarithmic scale ($\log_{10}(Z/Z_\odot)$) to express the metallicity at a certain shell, where $Z_\odot$ is the solar metallicity; we adopt $Z_\odot = 0.0127$ (Asplund et al. 2005). This way of calculating the metallicity is common in theoretical works. We note, however, that computing instead the oxygen to hydrogen abundance ratio (commonly used in observational works) gives effectively the same results.

3 THE EFFECT OF $\dot{M}_{\rm accr}$ ON THE GAS METALLICITY GRADIENTS

In this section, we present correlations between several galaxy properties obtained by the EAGLE simulations Ref-L100N1504 and Recal-L25N752, i.e. stellar mass, $\dot{M}_{\rm accr}$, SFR and neutral gas fraction, and how they correlate with the RMPs. This is done at $z = 0$ and 1. The analysis has also been performed for redshifts in between, which produce consistent results. Hence, for the sake of conciseness, we only show $z = 0, 1$.

3.1 The connection between metallicity, stellar mass and $\dot{M}_{\rm accr}$

Fig. 1 shows the gas metallicity vs. stellar mass relation at redshift $z = 0$ (top panel) and $z = 1$ (bottom panel) for a combined sample of galaxies from the Recal-L25N752 and Ref-L100N1504 simulations, described in Section 2. In this case, the gas metallicity is estimated from all the SF gas particles within 30 kpc from the centre of potential of the galaxy (this is the typical radius in which the integral properties of galaxies are calculated in the EAGLE simulations; see S15 for details). Median values of the gas metallicity are shown as solid lines, while the dashed lines depict the 16$^{\rm th}$ and 84$^{\rm th}$ percentiles. Coloured pixels show the median $\dot{M}_{\rm accr}$ of galaxies in bins of 0.25 dex in stellar mass and metallicity.

As expected, the gas metallicity increases with stellar mass until a threshold mass above which the metallicity saturates or even decreases. This threshold mass increases with redshift from $\approx 10^{10}\,{\rm M}_\odot$ at $z = 0$ to $10^{11}\,{\rm M}_\odot$ at $z = 1$. The normalisation of the MZR also increases with decreasing redshift, and its shape (in terms of a slope of the relation) changes with redshift as well. Thus, the MZR evolves in normalisation and shape, implying that a galaxy's stellar mass and chemical abundance evolve at different rates. This has been reported by Guo et al. (2016) for the Ref-L100N1504 simulation and by De Rossi et al. (2017) for Recal-L25N752. This evolution in normalisation is a natural success of the EAGLE simulations and generally not easily obtained in other simulations (see Collacchioni et al. 2018 for a discussion). It is interesting to note that, at fixed redshift, galaxies with higher stellar mass also have a higher $\dot{M}_{\rm accr}$, on average. This positive correlation is tight (about ~ 0.5 dex of dispersion) at all redshifts analysed in this work, and it is in agreement with previous theoretical work (e.g. van de Voort et al. 2011; Mollá et al. 2016; Correa et al. 2018).

From Fig. 1 it can also be seen that, at fixed stellar mass, the gas metallicity increases as $\dot{M}_{\rm accr}$ decreases, regardless of the redshift considered. This trend resembles the observed fundamental mass-metallicity relation plane (Mannucci et al. 2010; Lara-López et al. 2010), which correlates the metallicity, the stellar mass and the SFR in the sense that at fixed stellar mass the metallicity increases as the SFR decreases. The existence of this relation in EAGLE was demonstrated and discussed by De Rossi et al. (2017) and Matthee & Schaye (2018). In this scenario, the accretion of pristine gas has the dual effect of diluting the gas metallicity and triggering star formation (Troncoso et al. 2014). However, the fact that De Rossi et al. (2017) found a stronger anti-correlation between sSFR and metallicity in simulations with stronger stellar feedback indicates that outflows, which preferentially eject metals, also play an important role.

Galaxies have lower $\dot{M}_{\rm accr}$ as redshift decreases (at fixed stellar mass), showing an evolution with time. This is expected as the overall gas accretion rate onto halos, and therefore onto galaxies, decreases with time (Correa et al. 2018). However, it is important to emphasise that large differences are expected between $\dot{M}_{\rm accr}$ onto haloes and onto galaxies (e.g. van de Voort et al. 2011; van de Voort 2017; Nelson et al. 2013, 2019). The interplay between $\dot{M}_{\rm accr}$ and SFR will be analysed in Section 3.5.

3.2 The relation between the RMP and $\dot{M}_{\rm accr}$

The aim of this work is to get a better understanding of how $\dot{M}_{\rm accr}$ and other galaxy properties affect the RMPs. As was discussed in Section 1, the slope of the RMP measured over the whole galaxy does not depend on stellar mass or the environment in which the galaxy is immersed, particularly in the EAGLE simulations (Tissera et al. 2019). However, since we are interested in finding out whether there is a preferential radius below/above which the profiles are significantly affected by gas accretion, we divide them into several regions and analyse the corresponding slopes instead of analysing a single slope of the RMP. We measure the power-law slope of the RMP, α, in regions defined by the radii that contain half of the stellar mass of the galaxy, referred to as r_{50}. The benefit of using the stellar effective radius is that we obtain α in regions that one would consider "inner" or "outer" regardless of the physical size of the galaxy. We measure α in two regions: $r < r_{50}$ and $1 < r/r_{50} < 5$. We refer to these regions as inner and outer regions, respectively. We do this

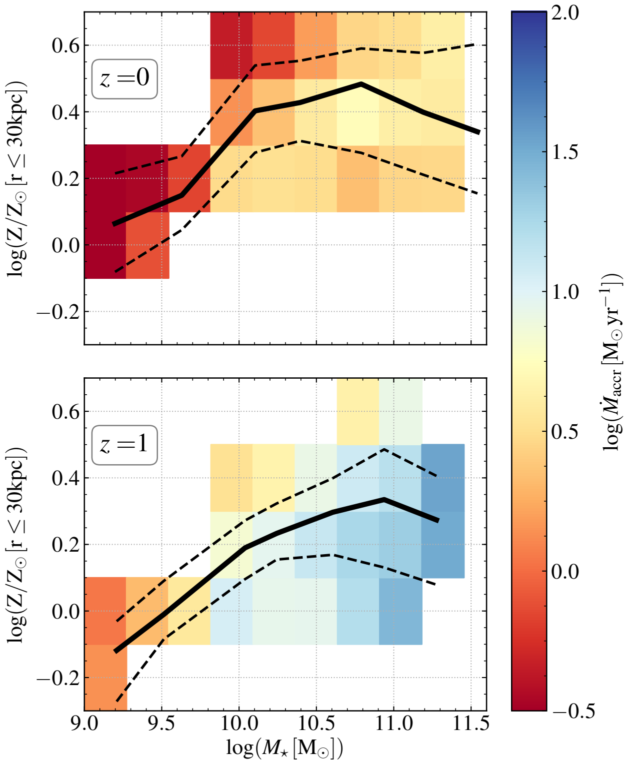

Figure 1. Stellar mass–gas metallicity relation (MZR) at $z = 0$ (top panel) and $z = 1$ (bottom panel) for galaxies in a combined simulated sample (combining the galaxy samples of the Recal-L25N752 and Ref-L100N1504 simulations; see details in Section 2). The gas metallicity is estimated using all the SF gas particles within 30 kpc from the centre of potential of the galaxy. For each panel, solid and dashed lines represent the median and $16^{\rm th}$ – $84^{\rm th}$ percentiles, respectively. At fixed redshift, galaxies with higher stellar mass show higher gas metallicity. At fixed stellar mass, galaxies show a higher gas metallicity at lower redshift. At fixed stellar mass and redshift, the metallicity is anti-correlated with $\dot{M}_{\rm accr}$. Coloured pixels represent the median $\dot{M}_{\rm accr}$ of the galaxies in bins of stellar mass and metallicity (containing at least 10 galaxies). Galaxies with higher stellar mass show higher $\dot{M}_{\rm accr}$, with $\dot{M}_{\rm accr}$ values decreasing as redshift decreases.

by using a linear fit in the space of $\log(Z/Z_\odot)$-r, as follows

$$\log_{10}(Z/Z_\odot) = \alpha \times r + \log_{10}(Z_0/Z_\odot), \quad (2)$$

where Z is the gas metallicity defined by Eq. 1, α is the slope we want to study (in units of dex kpc^{-1}), and Z_0 is the normalisation of the fit. We do not need the latter for the purpose of this work (in addition, it is very sensitive to the calibrator used to measure the metallicity, Ellison et al. 2008; Kewley & Ellison 2008).

Tissera et al. (2019), also using EAGLE, found that the slope of the gas metallicity profile correlates strongly with the half-neutral gas mass size radius (i.e., the radius that contains half of the neutral, i.e. atomic plus molecular, gas mass); but that the half-stellar mass radius plays a small role. This suggests that the effective radius of the neutral gas content would be a more appropriate property to study the radial metallicity profile (RMP). However, this property is only rarely available in observations and more difficult to define robustly. For example, observations of HI have shown that integrating longer, which allows to push towards lower HI column densities, continues to reveal HI, making the half-gas mass radius sensitivity-dependent (e.g. Oosterloo et al. 2007; Heald et al. 2011; Kamphuis et al. 2013). The stellar r_{50} is a well defined quantity that can be measured robustly for hundreds of thousands of galaxies (see Lange et al. 2016 for an example in the nearby Universe).

Fig. 2 shows the relation between the slope of the RMP in the inner (left) and outer (right) regions of EAGLE galaxies as a function of $\dot{M}_{\rm accr}$ at $z \leq 1$. Solid and dashed lines show the median values and $16^{\rm th}$ – $84^{\rm th}$ percentiles, respectively. Results for both simulations are shown separately using different colours. There is a small offset between the two simulations in this figure, which is not surprising as for Recal-L25N752 we are including all galaxies with stellar masses $M_\star \geq 10^9\,{\rm M}_\odot$, while for the Ref-L100N1504 simulation we limit the sample to galaxies with stellar masses $M_\star \geq 10^{10}\,{\rm M}_\odot$. We show later that eliminating the dependence on stellar mass brings the two simulations into agreement.

For the inner region, it can be seen that galaxies with a higher $\dot{M}_{\rm accr}$ display more negative RMP slopes α, with 1σ scatter of ≈ 0.1 dex kpc^{-1}. The anti-correlation between α and $\dot{M}_{\rm accr}$ is present in both simulations, although the trend is stronger for Recal-L25N752. This trend is seen at all redshifts studied. A simple physical picture to interpret this trend would be the accreted gas having lower metallicity than the interstellar medium in the galaxy, and hence diluting the gas as it falls onto the disk. This would steepen the RMP because conservation of specific angular momentum will cause the accreted gas to settle in the outskirts of galaxies (see Tissera et al. 2019 for an analysis of this scenario in EAGLE). Another explanation is that the correlation in Fig. 2 may be caused by these two galaxy properties correlating with a third, more fundamental one. We explore this in upcoming sections.

In the outer regions, $1 < r/r_{50} < 5$, we find that α stays close to ≈ -0.5 dex kpc^{-1}, however the correlation is dominated by a large scatter ($\gtrsim 1$ dex). The large scatter is likely caused by the outer regions of the interstellar medium having too small number of SF gas particles to measure the value of α robustly, making the measurement shot-noise dominated. Note that the values of r_{50} are usually in the range $\approx 3 - 10$ kpc and, in addition to the radial decline of the gas surface density (Bahé et al. 2016), the SF gas abundance drops considerably in the outer disk.

Besides the effect of shot noise, it is possible that the large scatter is in part due to some physical process. The environment in which the galaxies are immersed could be modifying the RMP at $r/r_{50} > 1$, as the outer parts of a galaxy tend to be more sensitive to gravitational interactions with neighbours. To explore this, we analysed the slopes of those galaxies that suffered a major merger since the previous snapshot (i.e., galaxies that had more than one progenitor of $M_\star \gtrsim 10^8$ M$_\odot$). We find that only ≈ 10 per cent of our sample had experienced a recent merger event, and that the slopes α in the three regions for this set of galaxies are very similar to the overall sample, indicating that galaxy mergers do not significantly affect the RMPs of galaxies. The flattening of the RMPs of galaxies in the outer

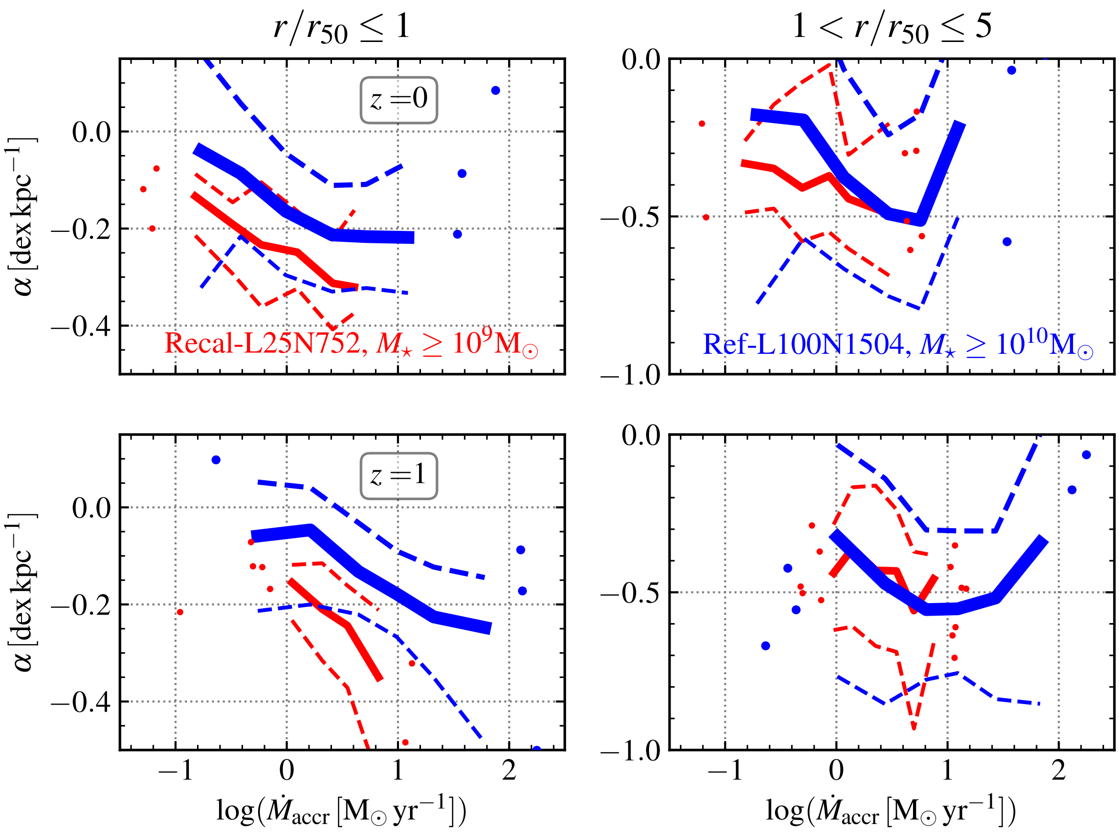

Figure 2. Median values of the RMP slopes, α, for each simulation used in this work as a function of $\dot{M}_{accr}$. Top and bottom panels show galaxies at $z = 0$ and $z = 1$, respectively. Left and right panels depict different regions of the galaxies, as labelled. Galaxies are colour-coded by the simulation they are generated with, being red for Recal-L25N752 and blue for Ref-L100N1504. Dashed lines depict the $16^{th} - 84^{th}$ percentiles. We show individual galaxies where bins have < 10 objects (circles). The RMP slope in the inner region ($r/r_{50} \leq 1$) is negative and it is tightly correlated with $\dot{M}_{accr}$ for both simulations at all redshifts analysed, becoming more negative for higher $\dot{M}_{accr}$. The Recal-L25N752 simulation shows a more negative slope, especially for higher values of $\dot{M}_{accr}$. At larger radii ($1 < r/r_{50} \leq 5$), we find a weaker correlation between α and $\dot{M}_{accr}$ with much larger scatter, with values of $\alpha \approx -0.5$. As explained in Section 2.2, the cuts in stellar mass for our galaxy samples are $M_\star \geq 10^9$ M$_\odot$ for Recal-L25N752 and $M_\star \geq 10^{10}$ M$_\odot$ for Ref-L100N1504. The difference in mass accounts for most of the difference between the simulations (see Section 3.3). Note that the $y-$axis range changes from the left to the right panels, which is done to better highlight the values spanned by the data.

regions could also be due to the gas metallicity of the interstellar medium reaching that of the halo gas, which may act as a floor to the metallicity. We currently cannot disentangle these explanations because of the small number of SF gas particles we generally have in the outer parts of the galaxies. Higher-resolution simulations would be required for such a detailed study and from now on we will therefore focus on the inner RMP slope.

3.3 The relation between the RMP and stellar mass

Fig. 3 shows the RMP inner slope, α, as a function of stellar mass. Both simulations display an anti-correlation so that more negative α are associated with more massive galaxies. This may seem at first sight in contradiction to the results of Tissera et al. (2019), who also used EAGLE, but the main difference is that here we show α measured within r_{50} while Tissera et al. (2019) measured a single α for the whole galaxy.

The two simulations analysed here, Recal-L25N752 and Ref-L100N1504, are offset at fixed mass, suggesting that stellar mass is not the primary property determining α.

We quantify which property, $\dot{M}_{accr}$ or stellar mass, shows a stronger correlation with the inner slope α via the Spearman's rank-order correlation coefficient (R_s), finding that $\dot{M}_{accr}$ gives absolute values that are similar (Recal-L25N752) or larger (Ref-L100N1504, above ≈ 0.1) than those obtained with stellar mass for all redshifts. Hence, in terms of scatter, α is better correlated with $\dot{M}_{accr}$ than with stellar mass.

3.4 The relation between the RMP and $\dot{M}_{accr}$ at fixed mass

We show in Fig. 4 the residuals of the α-$M_\star$ relation ($\Delta\alpha$) as a function of the residuals of the $\dot{M}_{accr}$-$M_\star$ relation ($\Delta\dot{M}_{accr}$). We define these residuals as follows

$$\Delta X = X - \mathrm{med}(X), \quad (3)$$

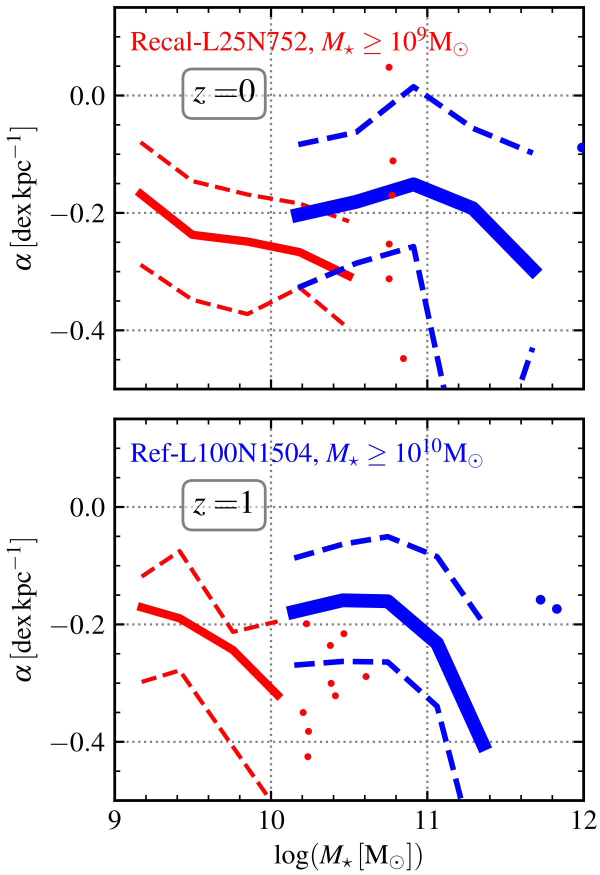

Figure 3. The median relation of the slope of the inner RMP, α, as a function of the stellar mass, $M_\star$. Top and bottom panels show galaxies at $z = 0$ and $z = 1$, respectively. The Recal-L25N752 simulation is shown with thin red lines, while the Recal-L25N752 simulation is shown with thick blue lines. In all cases, dashed lines depict the $16^{\rm th}-84^{\rm th}$ percentiles, and individual galaxies are shown with circles where bins have < 10 objects.

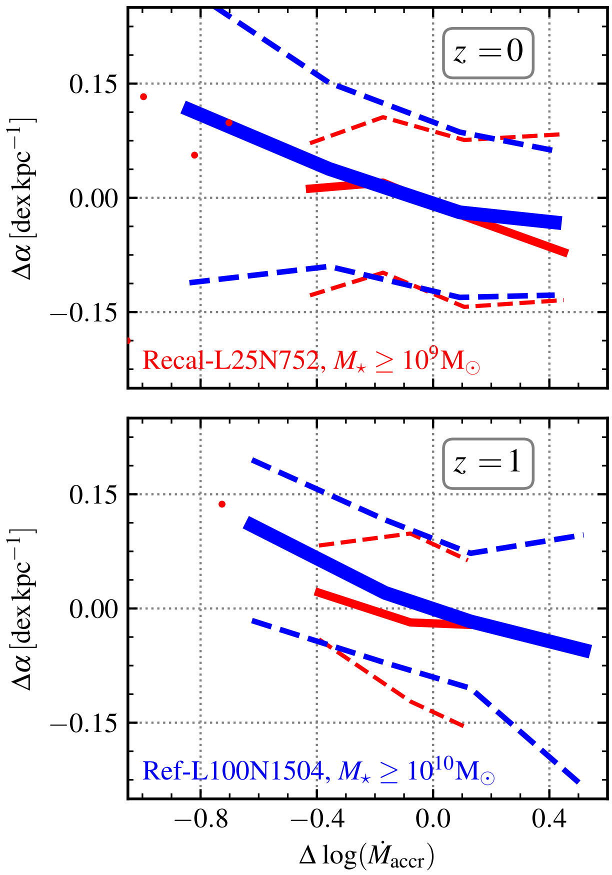

Figure 4. The residuals of the α-$M_\star$ relation as a function of the residuals of the $\dot{M}_{\rm accr}$-$M_\star$ relation, with α being the inner slope ($r/r_{50} \leq 1$) of the RMP. Top and bottom panels show galaxies at $z = 0$ and 1, respectively. Red and blue represent the Recal-L25N752 and Ref-L100N1504 simulations, respectively. The $16^{\rm th}-84^{\rm th}$ percentiles are depicted as dashed lines, and solid lines show medians. We show individual galaxies where bins have < 10 objects (red symbols). Having eliminated the dependence on stellar mass, we still see a very strong anti-correlation between α and $\dot{M}_{\rm accr}$, indicating this to be independent of stellar mass. The two simulations are in good agreement.

where X is the property of interest of a galaxy, and med(X) is the median value at the stellar mass of the galaxy.

By doing this calculation, we eliminate the stellar mass dependence from both axes. We find that the anti-correlation between $\Delta\alpha$ and $\Delta\dot{M}_{\rm accr}$ remains. We conclude that, at least for the inner regions, galaxies of fixed mass with a higher $\dot{M}_{\rm accr}$ display steeper (negative) RMPs. Although there is a general expectation that higher $\dot{M}_{\rm accr}$ can lead to changes in the RMP, to our knowledge this is the first time such results are quantified in cosmological simulations. Also note that for the residuals in Fig. 4 we do not see any differences between the standard and higher resolution EAGLE simulations, suggesting that the differences seen in Fig. 2 were due to differences in their stellar mass distributions.

3.5 The relation between the SFR, $\dot{M}_{\rm accr}$ and the RMP

Observationally, measuring $\dot{M}_{\rm accr}$ is very difficult as the gas is expected to have a low density and hence be very faint (e.g. Fox & Davé 2017). On the other hand, the integrated SFR of a galaxy is much easier to infer and is expected to be closely correlated with $\dot{M}_{\rm accr}$. In "equilibrium models", where $\dot{M}_{\rm accr}$ is perfectly balanced by the combination of SFR and outflow rates, the SFR can be directly computed from $\dot{M}_{\rm accr}$ and the mass loading parameter (the ratio between the outflow rate and SFR), which is typically set to ≈ 1 to predict the SFR and gas metallicities of galaxies (e.g. Davé et al. 2012; Lilly et al. 2013). Under the assumption of equilibrium, the SFR can then be used as a proxy for $\dot{M}_{\rm accr}$. If this is the case, one would expect the correlations discussed in Section 3.2 to also extend to the SFRs of galaxies. On the other hand, if what we are measuring in EAGLE is driven by the metal enrichment of the ISM due to recently formed stars (which would be aided by the accretion of gas), then one could imagine that the SFR may be the more fundamental parameter causing the change of the slope α rather than $\dot{M}_{\rm accr}$. This could be an interesting outcome since there is still debate as to whether there is a positive, negative or even null correlation between α and the SFR (see Section 1).

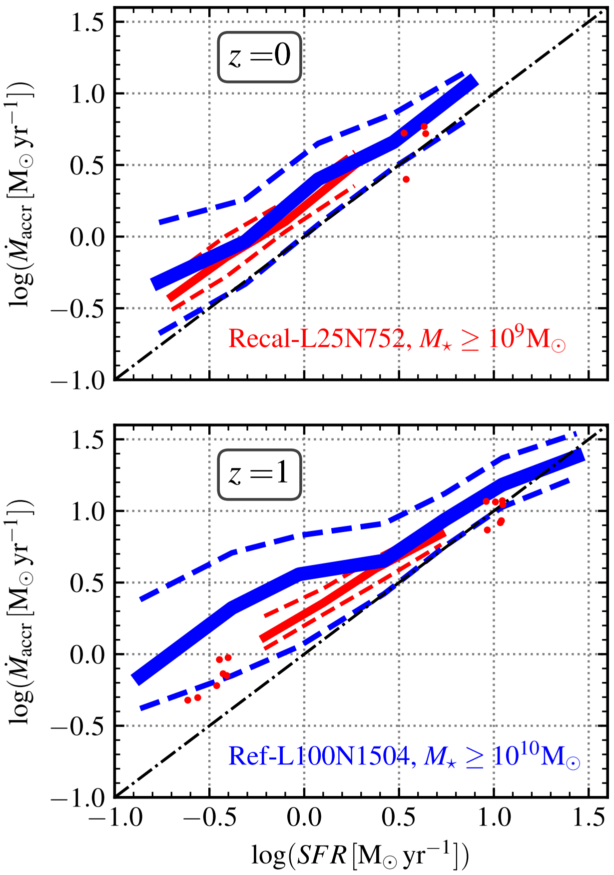

Figure 5. $\dot{M}_{\rm accr}$ as a function of the SFR of galaxies in the Recal-L25N752 (blue) and Ref-L100N1504 (red) simulations. Top and bottom panels show EAGLE galaxies at $z = 0$ and 1, respectively. The $16^{\rm th} - 84^{\rm th}$ percentiles are shown as dashed lines. We show individual galaxies in bins with < 10 objects as symbols. The dot-dashed lines show the 1:1 relation. We remind the reader that Recal-L25N752 galaxies were selected to have $M_\star \geq 10^9$ M$_\odot$, while Ref-L100N1504 galaxies were selected to have $M_\star \geq 10^{10}$ M$_\odot$. Both simulations display a positive and tight correlation between $\dot{M}_{\rm accr}$ and SFR. Also, at fixed SFR, galaxies display a weak decrease in their $\dot{M}_{\rm accr}$ of $\approx 0.2 - 0.3$ dex from $z = 1$ to 0.

Both of these two scenarios would result in an anti-correlation between α and the SFR, but in the former case one expects the scatter to be larger than for the relation between α and $\dot{M}_{\rm accr}$, while in the latter the opposite would be a more natural outcome. To disentangle between these two cases, we study the same correlations of Fig. 2 and 4, but for the SFRs of galaxies.

Before doing so, we verify the existence of a tight correlation between $\dot{M}_{\rm accr}$ and SFR in Fig. 5. In agreement with the expectation of the equilibrium models described above, we find a strong correlation between $\dot{M}_{\rm accr}$ and the SFR at all redshifts studied here, with a 1σ scatter $\lesssim 0.5$ dex. The scatter significantly decreases with SFR, from ≈ 0.5 dex at SFR $\lesssim 0.45\,{\rm M_\odot\,yr^{-1}}$ to ≈ 0.1 dex at SFR $\gtrsim 6\,{\rm M_\odot\,yr^{-1}}$. Although we do expect an overall correlation between the SFR and $\dot{M}_{\rm accr}$, the scatter here may be artificially small considering our definition of gas accretion, which is based on gas accretion that leads to SF (see Section 2.1 and Mitchell et al. in prep. for details). Interestingly, the predicted median relation evolves only weakly with redshift, at least at $z \leq 1$, with differences of $\lesssim 0.3$ dex between $z = 1$ and 0 at fixed SFR.

The left panel of Fig. 6 shows the slope of the RMP in the inner regions ($r/r_{50} < 1$) as a function of the SFR. This relation shows a similar trend and scatter as the one with $\dot{M}_{\rm accr}$ (see Fig. 2). As we did in Section 3.3, we quantify the correlations, finding the α-$\dot{M}_{\rm accr}$ correlation to give a similar (Recal-L25N752) or higher (Ref-L100N1504) R$_{\rm s}$ by ~ 0.1 than the α-SFR relation (again, $\dot{M}_{\rm accr}$ reaching R$_{\rm s}$ values more negative than −0.3), suggesting that the more fundamental correlation is that with $\dot{M}_{\rm accr}$. Tissera et al. (2019) showed that EAGLE galaxies with more negative slopes tend to have a larger fraction of their stars formed recently, consistent with the fact that there has been more gas accretion leading to such star formation activity, and with the clear anti-correlation we find here between α and the SFR. We caution, however, that Tissera et al. (2019) measured a single slope of the RMP rather than separating it into different regions of the disk.

As was done for $\dot{M}_{\rm accr}$, we remove the dependence on stellar mass by studying the residuals of the α-$M_\star$ relation as a function of the residuals of the SFR-$M_\star$ relation (see Eq. 3) in the right panel of Fig. 6 for $z = 0$ and 1. As explained in Section 3.2, the residuals are constructed as the difference between the property (i.e., slopes or SFR) and the median at the stellar mass of the galaxy. As was the case for Fig. 4, controlling for stellar mass brings the two simulations into agreement. The simulation Recal-L25N752 displays a weak anti-correlation between $\Delta\,\alpha$ and $\Delta\,$SFR (R$_{\rm s}$, the Spearman's rank-order correlation coefficient, of ≈ -0.2), similar to the anti-correlation between $\Delta\,\alpha$ and $\Delta\,\dot{M}_{\rm accr}$ (Fig. 4). However, the simulation Ref-L100N1504 shows a stronger anti-correlation with R$_{\rm s}$ ≈ -0.3. These results suggest that the α-SFR relation is a byproduct of the other properties coming into play, such as that of $\dot{M}_{\rm accr}$ and stellar mass. Therefore, we conclude that the inner RMP slope is primarily set by the gas accretion rate rather than by the SFR.

3.6 The relation between the RMP and the gas fraction

In the so-called "equilibrium model", $\dot{M}_{\rm accr}$ regulates the gas content, SFR and metallicity of galaxies. The gas fraction of a galaxy is therefore expected to be a tracer of gas accretion (modulo the timescale to convert gas into stars and outflows). The gas fraction is attractive as is more readily available in observations than $\dot{M}_{\rm accr}$, and can be linked back to the latter (although under some assumptions). Hence, one would expect that a galaxy formation simulation which overall captures the nature of star-forming galaxies, produces a relation between a galaxy's gas metallicity and gas fraction. Here, we explore the relation between the RMP and the gas fraction of galaxies.

We use the neutral gas fraction measurement of Lagos et al. (2016), defined as the neutral gas mass within 30 kpc, $M_{\rm HI} + M_{\rm H_2}$, over the sum of the former and baryon mass in the same aperture, $M_\star + M_{\rm HI} + M_{\rm H_2}$. The neutral gas mass is found by applying the ionised-to-neutral gas separation in post-processing following Rahmati et al. (2013) (see Lagos et al. 2015 for details of the subgrid phase partition of gas particles).

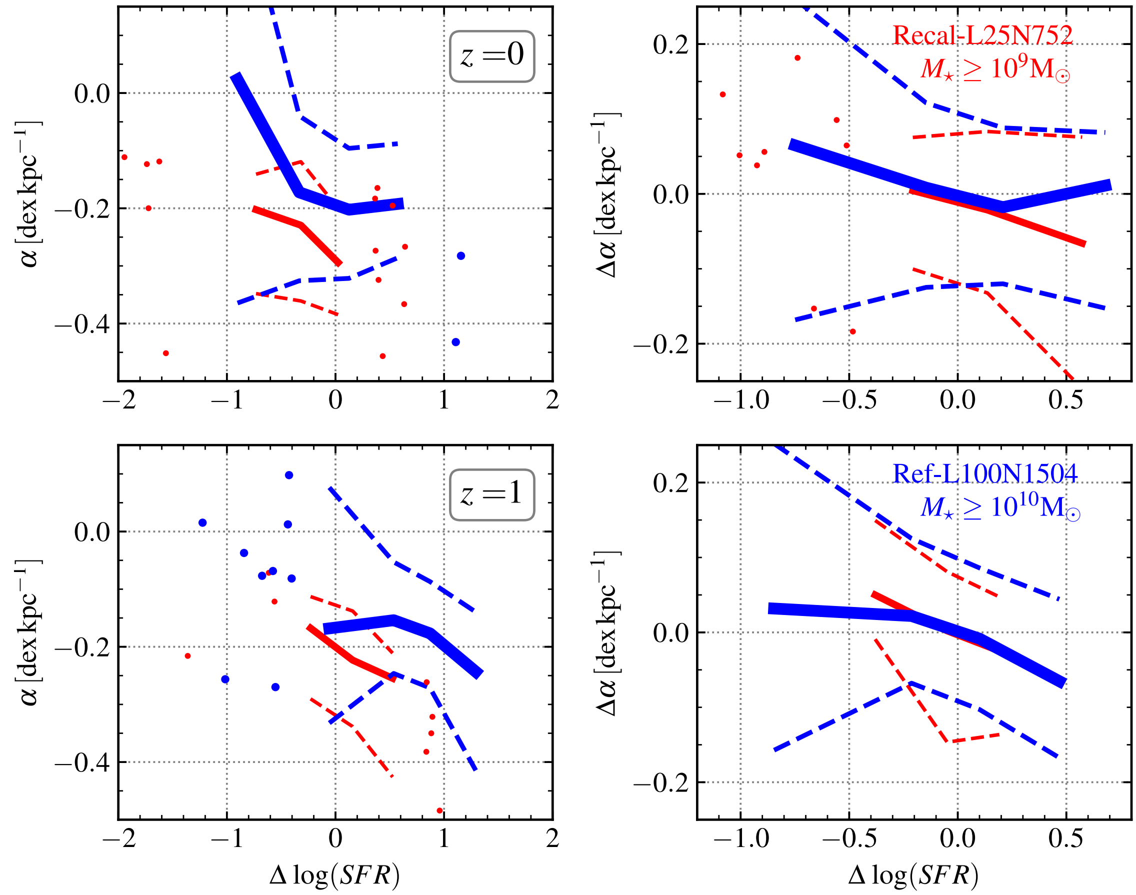

Figure 6. *Left:* Solid lines show median values of inner ($r/r_{50} \leq 1$) RMP slope aas a function of the SFR at redshift $z = 0$ (top panel) and $z = 1$ (bottom panel), for the Ref-L100N1504 (blue) and Recal-L25N752 (red) simulations. A similar anti-correlation is obtained as for $\alpha - \dot{M}_{\rm accr}$ (left panel of Fig. 2). *Right:* Solid lines show median values of the residuals of the relation between the inner ($r/r_{50} \leq 1$) RMP slope and stellar mass, as a function of the residuals of the SFR and the stellar mass. Redshifts are as labelled. Once we control for stellar mass (right panels), the anti-correlation is weaker than that between $\Delta\alpha$ and $\Delta \log(\dot{M}_{\rm accr})$ shown in Fig. 4. This suggests that the anti-correlation between the slope of the RMP and the SFR is only a byproduct of the anti-correlation between the RMP slope and $\dot{M}_{\rm accr}$. *All panels:* The $16^{\rm th} - 84^{\rm th}$ percentiles are depicted with dashed lines. We show individual galaxies where bins have < 10 objects (circles).

The left column of Fig. 7 shows the RMP slope at $r < r_{50}$ as a function of the neutral gas fraction at $z = 0$ and 1 for the Ref-L100N1504 (blue) and Recal-L25N752 (red) simulations. If we first look at the Ref-L100N1504 simulation, we see that there is a tendency for the RMP to decrease with radius more steeply as the gas fraction increases for all redshifts studied. This is because higher gas fractions are associated with higher $\dot{M}_{\rm accr}$. However, in the Recal-L25N752 simulation we see a reversal of that relation. This is because the gas fraction is strongly anti-correlated with stellar mass (see Fig. 1 in Lagos et al. 2016). Hence, it is necessary to remove the stellar mass dependence to unveil a possible correlation between the RMP and gas fraction.

The right column of Fig. 7 shows the relation between the residuals of the RMP slope and the residuals of the gas fraction ($\Delta f_{\rm gas}$) as previously defined in Eq. 3 (Section 3.2). The correlation is shown at $z = 0$ (top panel) and $z = 1$ (bottom panel). It is interesting to note that once the stellar mass dependence is removed, a strong anti-correlation is found, which is reminiscent of Fig. 4. This could be related to the fact that all the galaxy properties mentioned in this work (i.e. $\dot{M}_{\rm accr}$, SFR and $f_{\rm gas}$) modulate, but to different degrees, the RMP slope at fixed stellar mass.

We compute the Spearman's rank-order correlation coefficient R_s for the $\Delta\alpha - \Delta f_{\rm gas}$ relation ($R_{\rm s,gas}$) and compare it with that obtained for the $\Delta\alpha - \Delta$GAR relation ($R_{\rm s,accr}$). For both relations, R_s is similar for the simulations Ref-L100N1504 and Recal-L25N752, with values of ≈ -0.2 and ≈ -0.3, respectively. It is worth mentioning, though, that the absolute values of R_s indicate the α-$\dot{M}_{\rm accr}$ relation to be stronger than the $\alpha - f_{\rm gas}$ relation at all redshifts considered.

It is curious that the relation of the RMP slope with $f_{\rm gas}$ changes so much going from the left to the right panel of Fig. 7, compared to what happens with $\dot{M}_{\rm accr}$ (Figs. 2 and 4) and the SFR (Fig. 6). These large differences arise because the correlation between $\dot{M}_{\rm accr}$ and gas mass (HI +H_2) changes with stellar mass. The relation is positive at low stellar mass, but flattens or even inverts as the stellar mass increases. Hence, at low stellar masses ($M_\star \lesssim 10^{10}$ M$_\odot$), gas accretion mostly increases the gas fraction of the galaxy (which is the case of dwarf galaxies), while at high stellar masses ($M_\star \gtrsim 10^{10.5}$ M$_\odot$), gas accretion may trigger AGN

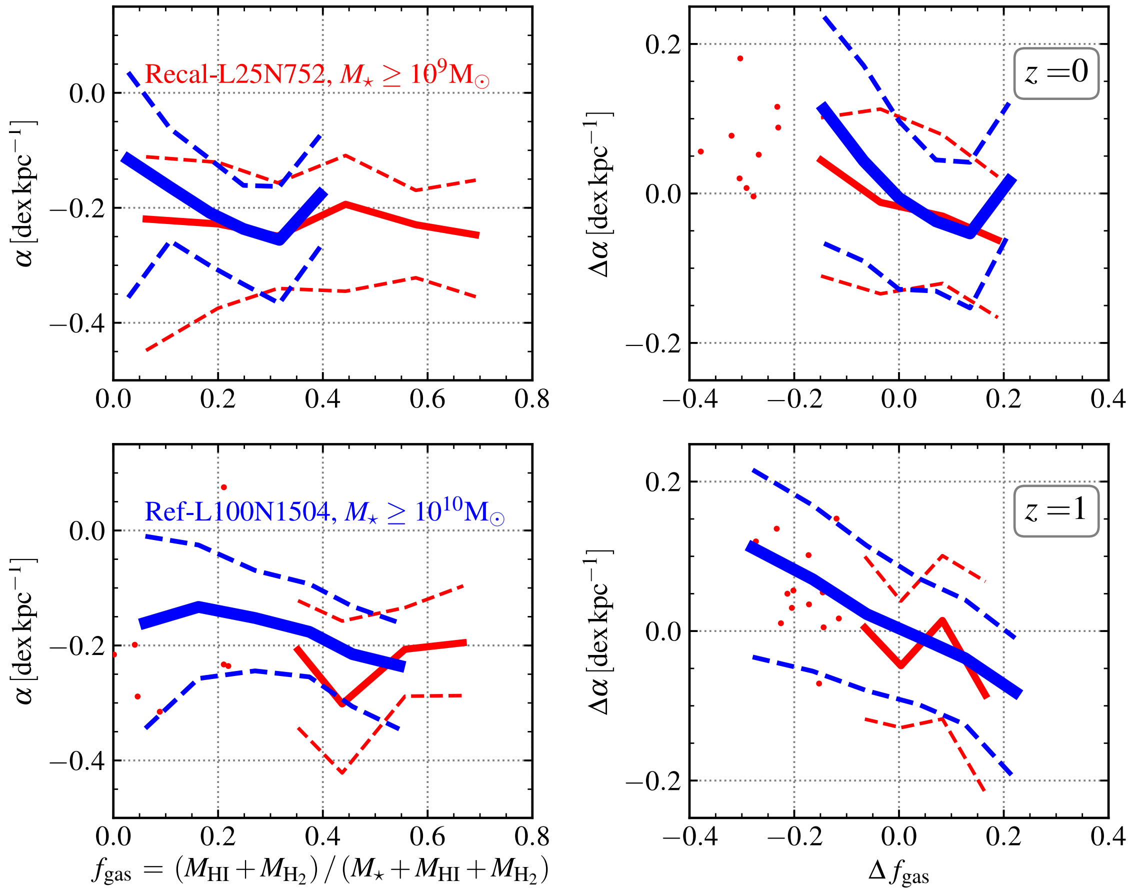

Figure 7. *Left:* Solid curves show median values of the inner ($r/r_{50} \leq 1$) RMP slope as a function of the neutral gas fraction $f_{\rm gas}$ at redshift $z = 0$ (top panel) and $z = 1$ (bottom panel), for the Ref-L100N1504 (blue) and Recal-L25N752 (red) simulations. A similar anti-correlation is observed as in Fig. 2 for the inner part. *Right:* Solid lines show median values of the residuals of the relation between the inner ($r/r_{50} \leq 1$) RMP slope and stellar mass, as a function of the residuals of the $f_{\rm gas}$ and the stellar mass. Redshifts are as labelled. As in Fig. 4, the inner region RMP slope displays an anti-correlation with $f_{\rm gas}$ even after eliminating the dependence on stellar mass. *All panels:* The $16^{\rm th}$ – $84^{\rm th}$ percentiles are depicted with dashed lines. We show the individual galaxies where bins have < 10 objects (red symbols).

feedback which then reduces the gas fraction. Thus, even though the relation between the RMP slope and $f_{\rm gas}$ gives us important constraints on the effect of gas accretion, it is neither as simple nor as direct a relation as the one we obtain between the RMP slope and $\dot{M}_{\rm accr}$. See Appendix B for the results when only considering the molecular gas component (H_2) for the gas fraction, which can be of use since atomic gas (i.e, HI) is currently not accessible in observations at $z \gtrsim 0.4$.

4 DISCUSSION

We showed in the previous sections (3.2 and 3.5) that the gas accretion plays an important role in shaping the inner slope of the RMP. We have also concluded that other galaxy properties, such as SFR, stellar mass and gas fraction, have a secondary role in the process of altering the slope, and are most likely driven by how these correlate with $\dot{M}_{\rm accr}$. To better visualise the effect of gas accretion on the RMP, we show in Fig. 8 the RMP of galaxies in bins of stellar mass and $\dot{M}_{\rm accr}$, for the Ref-L100N1504 simulation, at $z = 0$ (left) and $z = 1$ (right). The top panels show galaxies with stellar masses in the range of $M_\star/\mathrm{M}_\odot \in [10^{10}, 10^{10.3}]$, while bottom panels show a stellar mass range of $M_\star/\mathrm{M}_\odot \in [10^{10.3}, 10^{11}]$. We rank the $\dot{M}_{\rm accr}$ values and present the median RMPs of galaxies in three $\dot{M}_{\rm accr}$ percentiles: the bottom $25^{\rm th}$, between $40^{\rm th}$–$60^{\rm th}$, and the top $25^{\rm th}$. This allows us to compare galaxies in a way that is independent of the overall $\dot{M}_{\rm accr}$ evolution.

Galaxies with higher $\dot{M}_{\rm accr}$ show a steeper inner slope, independently of their stellar mass and redshift. In the stellar mass range 10^{10} – $10^{10.3}\,\mathrm{M}_\odot$ at $z = 0$ (top left panel in Fig. 8), galaxies have similar gas metallicities at the centre; however, galaxies with low $\dot{M}_{\rm accr}$ have RMPs with a flattened core that can extend to quite large radii ($r \approx 0.5\,r_{50}$), while galaxies with higher $\dot{M}_{\rm accr}$ do not show a core in their RMP, and instead fall off sharply. This behaviour, however, is not universal (the top right panel does not show such a sharp fall). Note that at large radii, $r \approx 10\,r_{50}$, galaxies display a flattening of their RMP, probably due to the ISM reaching the circum-galactic medium metallicity. The latter happens at systematically smaller radii for galaxies with high $\dot{M}_{\rm accr}$. In more massive galaxies (bottom left panel in Fig. 8), the flattened RMP core in galaxies of low $\dot{M}_{\rm accr}$ is

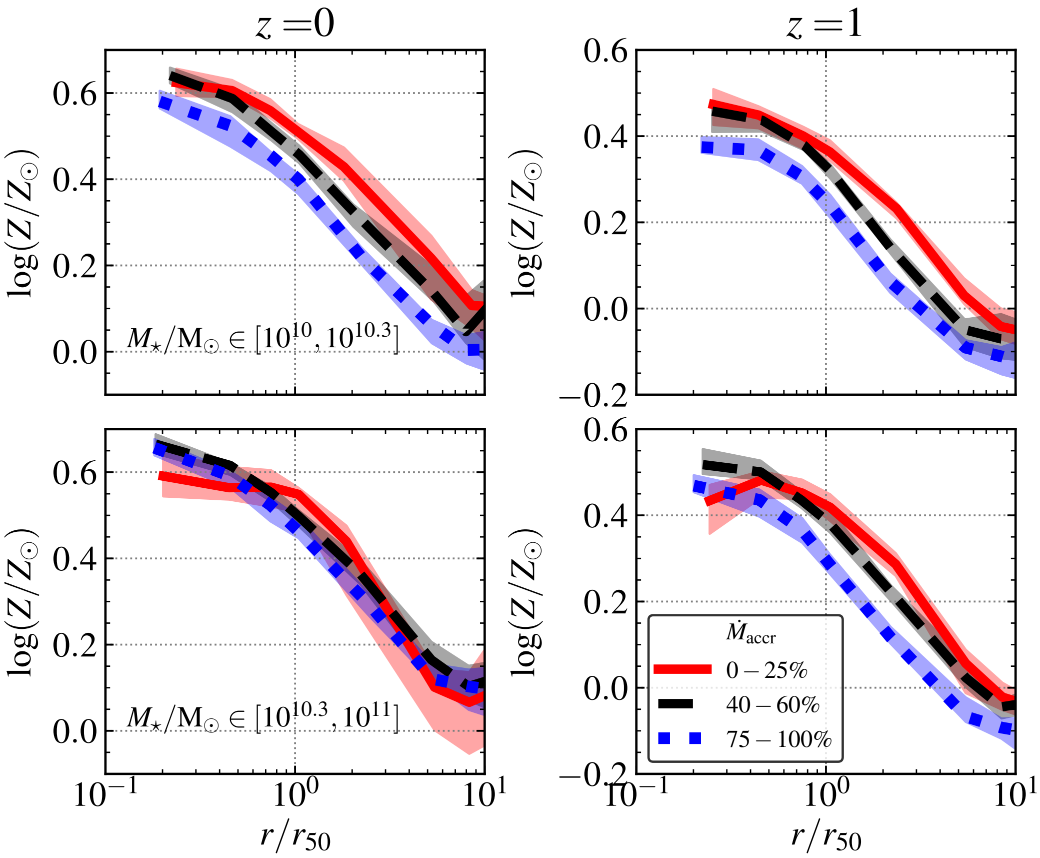

Figure 8. RMP at $z = 0$ (left column) and $z = 1$ (right column) for galaxies in the Ref-L100N1504 simulation. The upper panels show galaxies with a stellar mas of $M_\star/M_\odot \in [10^{10}, 10^{10.3}]$, while the bottom panels show the range $M_\star/M_\odot \in [10^{10.3}, 10^{11}]$. Different colours represent the percentiles of $\dot{M}_{accr}$, as labelled. The lines and shaded regions show the median RMP and its $16^{th} - 84^{th}$ percentiles, respectively. Galaxies with higher $\dot{M}_{accr}$ (dashed lines) show a steeper slope at $r < r_{50}$. Since the softening for the Ref-L100N1504 simulation is 0.7 kpc and we find average values of $r_{50} \approx 4.22$ kpc at $z = 0$ and $r_{50} \approx 3.11$ kpc at $z = 1$, the profiles will be resolved for $r/r_{50} \gtrsim 0.17$ and $r/r_{50} \gtrsim 0.23$, respectively. It is interesting to note that, at fixed stellar mass, there is a vertical offset of metallicity according to different values of $\dot{M}_{accr}$, as was discussed in Section 3.1.

even more prominent, reaching out to $r \approx r_{50}$, while the higher $\dot{M}_{accr}$ galaxies do not display a core. At $z = 1$ the main difference is that the gas metallicities are overall lower than at $z = 0$, and the differences in the normalisation of the RMPs at fixed stellar mass for different $\dot{M}_{accr}$ is larger.

Our analysis can also give insight into where the gas recently accreted onto the galaxy is. Galaxies with higher $\dot{M}_{accr}$ display steeper gradients in the internal parts. Thus, gas accretion appears to be diluting the metals in an outside-in fashion, which translates into more negative RMPs.

An important consideration to interpret the observed trends above is the way in which we measure $\dot{M}_{accr}$. Because we are specifically tracking particles that at the time of interest are star forming (those that have SFRs > 0), but were not in the galaxy in the previous timestep, it is natural to expect our measure to be biased towards gas accretion that leads to star formation and hence that leads to more important changes in the RMP in the centre (where most star formation takes place[3]). With this technique, we are therefore likely seeing the most effect the gas accretion can have on the internal RMP. However, our measurement of gas accretion is a lower limit as we are by construction ignoring the gas particles that join the ISM but are not related to star formation, as well as particles that were ejected in between snapshots.

Another important caveat to keep in mind is that we are radially averaging the effect of gas accretion, which simulations show is not necessarily axisymmetric. This may be washing out some of the more localised effects the gas accretion can have, particularly if it is strongly filamentary. In the future, we will study the gas accretion effects in the 2-dimensional gas metallicity distribution of galaxies with the aim of quantifying how much variation is expected in individual galaxies due to the generally asymmetric nature of gas accretion.

Despite these limitations, our work clearly establishes the important role of gas accretion in shaping the RMP of

[3] We remind the reader that this is done for ease of comparison with observational measurements, which typically use nebular emission lines that trace HII regions.

galaxies, which we are able to control for other effects, such as stellar mass and SFR variations, thanks to the statistics of the EAGLE simulations, finding that *gas accretion is the primary responsible for the slope of the RMP*. Note that metallicities, SFRs, and gas fractions were not used in the process of parameter tuning in EAGLE and hence, the result we present in this paper represents a true prediction of the simulation.

Our results establish some clear correlations that we would expect at fixed stellar mass: galaxies with steeper (more negative) RMPs at $r < r_{50}$ tend to have higher neutral gas fractions and $\dot{M}_{\rm accr}$ (the latter being more difficult to test).

Deep measurements of the HI content of galaxies that push down to low column densities, typical of the circumgalactic medium (Popping et al. 2009), together with metallicity gradient estimates from IFS surveys, will be an ideal combination to test our predictions. Instruments such as the Australian Square Kilometre Array (SKA) Pathfinder (ASKAP; Johnston et al. 2008) and the Karoo Array Telescope (MeerKAT; Booth et al. 2009), and in the future the SKA, will allow the former measurements, while instruments such as SAMI (Bryant et al. 2015), MUSE (Carton et al. 2018), and other IFS surveys, allow for the latter. Note that our results cannot be easily extrapolated to $z > 1$ as galaxy mergers are expected to become more common (as shown by Qu et al. 2017; Lagos et al. 2018 for EAGLE) and because our $\dot{M}_{\rm accr}$ ignores the gas that comes from galaxy mergers (as we are aiming to quantify "smooth" accretion), this may become an important shortfall. In addition, the $\dot{M}_{\rm accr}$ at $z \gtrsim 1$ is expected to be much more collimated and to penetrate down to the galaxy more easily than at $z \lesssim 1$ (e.g. Correa et al. 2018). This may have the effect of directly feeding the central regions of the galaxy rather than from outside-in, possibly driving the inverted RMP seen in observations at $z \approx 3-4$ (Troncoso et al. 2014; Cresci et al. 2010).

Recently, Patrício et al. (2019) presented observational measurements of the RMP of 3 strongly lensed galaxies at $z = 0.6$, 0.8 and 1, and reported these to have more negative α than $z = 0$ galaxies. This is consistent with our findings as galaxies at $z \approx 1$ have higher $\dot{M}_{\rm accr}$, therefore leading to more negative α. However, to confirm this observationally, a larger sample of galaxies is required to study the RMP at fixed stellar mass across cosmic time.

5 CONCLUSIONS

In this work we use two simulations from the EAGLE project, the reference large-volume, standard-resolution simulation of 100 Mpc on a side (Ref-L100N1504), and the recalibrated high-resolution simulation of 25 Mpc of a side (Recal-L25N752), to study how the slope of the radial metallicity profile (RMP) of galaxies, α, changes with the gas accretion rate ($\dot{M}_{\rm accr}$) and other galaxy properties. Because of the resolution limits of these simulations, we focus on galaxies with $M_{\star} \geq 10^{10}\,{\rm M}_{\odot}$ for the Ref-L100N1504 simulation, and $M_{\star} \geq 10^{9}\,{\rm M}_{\odot}$ for the Recal-L25N752 simulation. We also limit our study to central, star forming galaxies and to redshifts $z \leq 1$.

We use a particle tracking method to find the gas particles that are being accreted onto galaxies, including those that are converted into stars. We are especially interested in smooth accretion rather than accretion in the form of galaxy mergers, and hence we select only those gas particles that were not part of another galaxy in the previous simulation snapshots. Our aim is to find whether the $\dot{M}_{\rm accr}$ can be robustly connected to changes in the RMP as a primary driver, and hence controlling for differences in stellar mass and SFR is essential. The EAGLE simulations are an ideal tool for this purpose, as its combination of volume and resolution allows us to look into the internal structure of galaxies as well as providing us with enough statistics to explore galaxy properties at fixed stellar mass. Here, we focused only on central, star forming galaxies with at least 10 accreted gas particles in the last ≈ 100 Myr that come from sources other than galaxy mergers, at redshifts $z = 0$ and 1.

We summarise our conclusions as follows:

- The gas accretion rate is positively correlated with stellar mass (Fig. 1) and SFR (Fig. 5), at all redshifts studied. We also find that at fixed stellar mass, higher gas metallicity galaxies are associated with lower $\dot{M}_{\rm accr}$ (Fig. 1). Together, these results are consistent with the MZR-SFR relation (also called fundamental MZR in the literature; e.g. Mannucci et al. 2010).
- A tight negative correlation is found between the inner RMP slopes (measured within $r/r_{50} \leq 1$) and $\dot{M}_{\rm accr}$ (Fig. 2) at all redshifts studied. Galaxies with higher gas accretion rates tend to have steeper RMPs. Even though galaxies change their $\dot{M}_{\rm accr}$ with time at fixed stellar mass, this anti-correlation does not seem to evolve. At large radii, $r/r_{50} > 1$, we find a weak trend for the RMPs of galaxies to become flatter as $\dot{M}_{\rm accr}$ increases. However, this trend is characterised by a very large scatter caused by noise, which prevents us from drawing any strong conclusion. A higher resolution simulation would be required to confirm this trend.
- A clear anti-correlation between the inner RMP slope ($r/r_{50} \leq 1$) and $\dot{M}_{\rm accr}$ remains even when eliminating the dependence on stellar mass (Fig. 4).
- The SFR is not as strongly anti-correlated with the slope α as $\dot{M}_{\rm accr}$ is (Fig. 6), indicating that the latter is more fundamental in shaping the RMP.
- We also obtain a relation between the neutral gas fraction and the slope of the inner RMP (at $r/r_{50} \leq 1$; Fig. 7), but it is less clear than with $\dot{M}_{\rm accr}$. However, the gas fraction is a useful proxy as it is more readily accessible observationally than $\dot{M}_{\rm accr}$.
- When analysing the RMP binned by redshift and stellar mass, we see that galaxies with the lowest $\dot{M}_{\rm accr}$ show flatter inner slopes (even cored RMPs), while galaxies with the highest $\dot{M}_{\rm accr}$ display steeper negative slopes (Fig. 8).

In the future, we will aim to reveal what properties are causing the high scatter at $r/r_{50} > 1$, as well as studying galaxies in two dimensions rather than radially averaged (Marino et al. 2016; Trayford & Schaye 2019). Even though the assumptions made in the calculation of $\dot{M}_{\rm accr}$ are simple, it is clear that the latter plays a primary role in altering the RMPs of galaxies to a degree that we hope will be testable with a combination of sensitive IFS instruments, absorption line studies and deep HI observations, e.g. from local surveys such as SAMI (Bryant et al. 2015) and CALIFA (Sánchez et al. 2012), and in the near future the MUSE MAGPI[4] survey (MAGPI collaboration in prep.) at $z \approx 0.3$.

ACKNOWLEDGEMENTS

We thank Yannick Bahé for fruitful discussions and suggestions. We acknowledge the Virgo Consortium for making their simulation data available. The EAGLE simulations were performed using the DiRAC-2 facility at Durham, managed by the ICC, and the PRACE facility Curie based in France at TGCC, CEA, Bruyèresle-Châtel. FC acknowledges CONICET, Argentina, and the Australian Endeavour programme for their supporting fellowships. CL is funded by the Australian Research Council Centre of Excellence for All Sky Astrophysics in 3 Dimensions (ASTRO 3D), through project number CE170100013. The Cosmic Dawn Center is funded by the Danish National Research Foundation. SAC acknowledges funding from *Consejo Nacional de Investigaciones Científicas y Técnicas* (CONICET, PIP-0387), *Agencia Nacional de Promoción Científica y Tecnológica* (ANPCyT, PICT-2013-0317), and *Universidad Nacional de La Plata* (11-G150), Argentina. EW acknowledges support by the Australian Research Council Centre of Excellence for All Sky Astrophysics in 3 Dimensions (ASTRO 3D), through project number CE170100013.

REFERENCES

Asplund M., Grevesse N., Sauval A. J., 2005, in Barnes III T. G., Bash F. N., eds, Astronomical Society of the Pacific Conference Series Vol. 336, Cosmic Abundances as Records of Stellar Evolution and Nucleosynthesis. p. 25
Bahé Y. M., et al., 2016, MNRAS, 456, 1115
Behroozi P. S., Wechsler R. H., Wu H.-Y., 2013, ApJ, 762, 109
Belfiore F., et al., 2017, MNRAS, 469, 151
Boissier S., Prantzos N., 1999, MNRAS, 307, 857
Booth R. S., de Blok W. J. G., Jonas J. L., Fanaroff B., 2009, arXiv e-prints, p. arXiv:0910.2935
Bothwell M. S., Maiolino R., Peng Y., Cicone C., Griffith H., Wagg J., 2016, MNRAS, 455, 1156
Bryant J. J., et al., 2015, MNRAS, 447, 2857
Carton D., et al., 2015, MNRAS, 451, 210
Carton D., et al., 2018, MNRAS, 478, 4293
Chabrier G., 2003, PASP, 115, 763
Collacchioni F., Cora S. A., Lagos C. D. P., Vega-Martínez C. A., 2018, MNRAS, 481, 954
Correa C. A., Schaye J., van de Voort F., Duffy A. R., Wyithe J. S. B., 2018, MNRAS, 478, 255
Crain R. A., et al., 2015, MNRAS, 450, 1937
Crain R. A., et al., 2017, MNRAS, 464, 4204
Cresci G., Mannucci F., Maiolino R., Marconi A., Gnerucci A., Magrini L., 2010, Nature, 467, 811
Dalla Vecchia C., Schaye J., 2012, MNRAS, 426, 140
Davé R., Finlator K., Oppenheimer B. D., 2011, MNRAS, 416, 1354
Davé R., Finlator K., Oppenheimer B. D., 2012, MNRAS, 421, 98
Davis M., Efstathiou G., Frenk C. S., White S. D. M., 1985, ApJ, 292, 371
De Rossi M. E., Theuns T., Font A. S., McCarthy I. G., 2015, MNRAS, 452, 486
De Rossi M. E., Bower R. G., Font A. S., Schaye J., Theuns T., 2017, MNRAS, 472, 3354
Dolag K., Borgani S., Murante G., Springel V., 2009, MNRAS, 399, 497
Ellison S. L., Patton D. R., Simard L., McConnachie A. W., 2008, ApJ, 672, L107
Erroz-Ferrer S., et al., 2019, MNRAS, 484, 5009
Finlator K., 2017, in Fox A., Davé R., eds, Astrophysics and Space Science Library Vol. 430, Gas Accretion onto Galaxies. p. 221 (arXiv:1612.00802), doi:10.1007/978-3-319-52512-9_10
Finlator K., Davé R., 2008, MNRAS, 385, 2181
Fox A., Davé R., eds, 2017, Gas Accretion onto Galaxies Astrophysics and Space Science Library Vol. 430, doi:10.1007/978-3-319-52512-9.
Furlong M., et al., 2015, MNRAS, 450, 4486
Furlong M., et al., 2017, MNRAS, 465, 722
Guo Q., et al., 2016, MNRAS, 461, 3457
Heald G., et al., 2011, A&A, 526, A118
Ho I. T., Kudritzki R.-P., Kewley L. J., Zahid H. J., Dopita M. A., Bresolin F., Rupke D. S. N., 2015, MNRAS, 448, 2030
Hopkins P. F., Kereš D., Oñorbe J., Faucher-Giguère C.-A., Quataert E., Murray N., Bullock J. S., 2014, MNRAS, 445, 581
Jiang L., Helly J. C., Cole S., Frenk C. S., 2014, MNRAS, 440, 2115
Johnston S., et al., 2008, Experimental Astronomy, 22, 151
Kamphuis P., et al., 2013, MNRAS, 434, 2069
Kewley L. J., Ellison S. L., 2008, ApJ, 681, 1183
Lagos C. d. P., Lacey C. G., Baugh C. M., 2013, MNRAS, 436, 1787
Lagos C. d. P., et al., 2015, MNRAS, 452, 3815
Lagos C. d. P., et al., 2016, MNRAS, 459, 2632
Lagos C. d. P., et al., 2018, MNRAS, 473, 4956
Lange R., et al., 2016, MNRAS, 462, 1470
Lara-López M. A., et al., 2010, A&A, 521, L53
Lilly S. J., Carollo C. M., Pipino A., Renzini A., Peng Y., 2013, ApJ, 772, 119
Ludlow A. D., Schaye J., Schaller M., Richings J., 2019, MNRAS, 488, L123
Ma X., Hopkins P. F., Faucher-Giguère C.-A., Zolman N., Muratov A. L., Kereš D., Quataert E., 2016, MNRAS, 456, 2140
Ma X., Hopkins P. F., Feldmann R., Torrey P., Faucher-Giguère C.-A., Kereš D., 2017, MNRAS, 466, 4780
Maiolino R., Mannucci F., 2019, A&ARv, 27, 3
Maiolino R., et al., 2008, A&A, 488, 463
Mannucci F., Cresci G., Maiolino R., Marconi A., Gnerucci A., 2010, MNRAS, 408, 2115
Marino R. A., et al., 2016, A&A, 585, A47
Matthee J., Schaye J., 2018, MNRAS, 479, L34
McAlpine S., et al., 2016, Astronomy and Computing, 15, 72
McAlpine S., Bower R. G., Harrison C. M., Crain R. A., Schaller M., Schaye J., Theuns T., 2017, MNRAS, 468, 3395
Mollá M., Díaz Á. I., Gibson B. K., Cavichia O., López-Sánchez Á.-R., 2016, MNRAS, 462, 1329
Muratov A. L., et al., 2017, MNRAS, 468, 4170
Neistein E., Khochfar S., Dalla Vecchia C., Schaye J., 2012, MNRAS, 421, 3579
Nelson D., Vogelsberger M., Genel S., Sijacki D., Kereš D., Springel V., Hernquist L., 2013, MNRAS, 429, 3353
Nelson D., et al., 2019, arXiv e-prints,
Oosterloo T. A., Morganti R., Sadler E. M., van der Hulst T., Serra P., 2007, A&A, 465, 787
Patrício V., et al., 2019, arXiv e-prints, p. arXiv:1907.11586
Perez J., Michel-Dansac L., Tissera P. B., 2011, MNRAS, 417, 580
Planck Collaboration et al., 2014, A&A, 571, A1
Poetrodjojo H., et al., 2018, MNRAS, 479, 5235

[4] https://magpisurvey.org/

Popping A., Davé R., Braun R., Oppenheimer B. D., 2009, A&A, 504, 15
Qu Y., et al., 2017, MNRAS, 464, 1659
Rahmati A., Pawlik A. H., Raičević M., Schaye J., 2013, MNRAS, 430, 2427
Sánchez-Menguiano L., et al., 2016, A&A, 587, A70
Sánchez S. F., et al., 2012, A&A, 538, A8
Sánchez S. F., et al., 2013, A&A, 554, A58
Sánchez S. F., et al., 2014, A&A, 563, A49
Schaller M., Dalla Vecchia C., Schaye J., Bower R. G., Theuns T., Crain R. A., Furlong M., McCarthy I. G., 2015, MNRAS, 454, 2277
Schaye J., 2004, ApJ, 609, 667
Schaye J., Dalla Vecchia C., 2008, MNRAS, 383, 1210
Schaye J., et al., 2015, MNRAS, 446, 521
Sillero E., Tissera P. B., Lambas D. G., Michel-Dansac L., 2017, MNRAS, 472, 4404
Springel V., 2005, MNRAS, 364, 1105
Springel V., White S. D. M., Tormen G., Kauffmann G., 2001, MNRAS, 328, 726
Stott J. P., et al., 2014, MNRAS, 443, 2695
Tissera P. B., Pedrosa S. E., Sillero E., Vilchez J. M., 2016, MNRAS, 456, 2982
Tissera P. B., Rosas-Guevara Y., Bower R. G., Crain R. A., del P Lagos C., Schaller M., Schaye J., Theuns T., 2019, MNRAS, 482, 2208
Trayford J. W., Schaye J., 2019, MNRAS, 485, 5715
Trayford J. W., et al., 2015, MNRAS, 452, 2879
Tremonti C. A., et al., 2004, ApJ, 613, 898
Troncoso P., et al., 2014, A&A, 563, A58
Wiersma R. P. C., Schaye J., Smith B. D., 2009a, MNRAS, 393, 99
Wiersma R. P. C., Schaye J., Theuns T., Dalla Vecchia C., Tornatore L., 2009b, MNRAS, 399, 574
Wright R. J., Lagos C. d. P., Davies L. J. M., Power C., Trayford J. W., Wong O. I., 2019, MNRAS, 487, 3740
Wuyts E., et al., 2016, ApJ, 827, 74
Zahid H. J., Dima G. I., Kudritzki R.-P., Kewley L. J., Geller M. J., Hwang H. S., Silverman J. D., Kashino D., 2014, ApJ, 791, 130
Zinchenko I. A., Just A., Pilyugin L. S., Lara-Lopez M. A., 2019, A&A, 623, A7
van de Voort F., 2017, in Fox A., Davé R., eds, Astrophysics and Space Science Library Vol. 430, Gas Accretion onto Galaxies. p. 301 (arXiv:1612.00591), doi:10.1007/978-3-319-52512-9_13
van de Voort F., Schaye J., Booth C. M., Haas M. R., Dalla Vecchia C., 2011, MNRAS, 414, 2458

APPENDIX A: CONVERGENCE OF $\dot{M}_{\rm accr}$-RMP RELATION

Throughout this work, we consider central, star-forming galaxies with at least 10 star-forming gas particles that have been accreted (which were outside the galaxy ≈ 100 Myr ago). This minimum of particles translates to values of $\dot{M}_{\rm accr} \approx 9 \times 10^{-2}\,{\rm M_{\odot} yr^{-1}}$. Here, we assess the robustness of our findings to the minimum number of gas accreted particles allowed.

We show in Fig. A1 the relation between the RMP slope residuals, $\Delta\alpha$, and the $\dot{M}_{\rm accr}$ residuals, $\Delta\dot{M}_{\rm accr}$, for four SF gas particles minimum number cuts, from at least 1 particle to 100 particles, as labelled. We remind the reader that we define these residuals in Section 3.2. For the sake of clarity, we only show the 1σ scatter for our fiducial cut of 10 particles

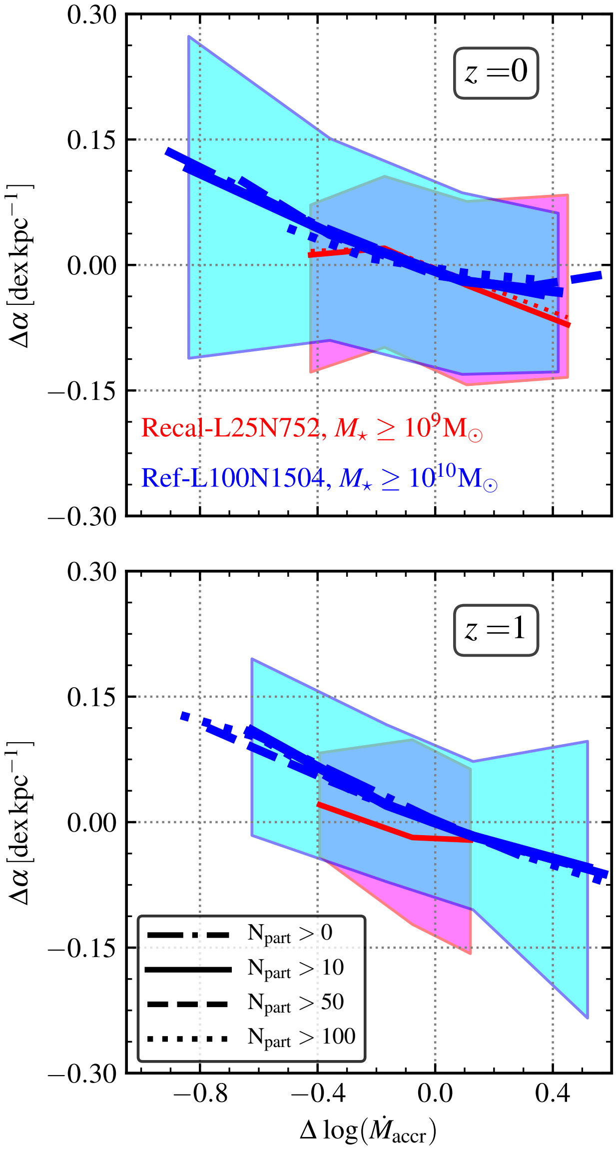

Figure A1. Same as Fig. 4, but now comparing different minimum number of gas particles of the accreted gas above which we include galaxies in our analysis. Solid, dashed and dotted lines show $\dot{M}_{\rm accr}$ in galaxies with ≥ 10, ≥ 50 and ≥ 100 gas particles of accreted gas, respectively. The errorbars show the 1σ percentiles and are shown only for the case of ≥ 10 gas particles, for clarity.

for both simulations (the magenta shaded region depicts the Recal-L25N752 simulation, while cyan represents the Ref-L100N1504 simulation).

We can see that for all redshifts analysed there is almost no difference between the four SF gas particles number cuts. It is interesting to further analyse the cases where galaxies have fewer than 10 accreted star-forming gas particles. For simulation Ref-L100N1504, 17 galaxies at $z = 0$ (≈ 10 per cent of the sample at this redshift) have fewer than 10 particles and we find them to follow the same trends reported in this manuscript. At $z = 1$, only one galaxy from this simulation is found to have fewer than 10 gas particles (it has $\dot{M}_{\rm accr} \approx 10^{-2.5}\,{\rm M_{\odot}/yr^{-1}}$ and $\alpha \approx 0.015$). On the contrary, simulation Recal-L25N752 does not have any central, star-forming galaxy with fewer than 10 accreted star-forming gas particles (at least until $z \leq 1$). We hence conclude that our results are robust to the chosen minimum number of gas particles for the accreted gas, above which we include galaxies in our analysis.

APPENDIX B: WHEN CONSIDERING ONLY MOLECULAR HYDROGEN IN THE GAS FRACTION

Since observationally it is easier to measure molecular gas H_2 than atomic hydrogen HI at $z \gtrsim 0.5$, we test if our conclusions from Section 3.6 might change if only considering the former.

Fig. B1 is a replica of Fig. 7, but with a twist in the definition of the gas fraction. Now, we consider the contribution of the H_2 and so we have that gas fraction is defined as $f_{\rm gas} = M_{\rm H_2}/(M_\star + M_{\rm H_2})$. At first sight, one of the differences is that the values of the $f_{\rm gas}$ drop considerably compare to our previous definition. This is due to the fact that $M_{\rm HI}$ is more abundant than the molecular component. Another interesting thing to stand out is that the maximum values of $f_{\rm gas}$ increases with redshift, showing why through observations is easier to measure the $M_{\rm H_2}$ at redshift $z \gtrsim 0.5$.

With this, we conclude that whether the definition of gas fraction involves H_2 or HI (not shown), the results we found in Section 3.6 remain the same.

This paper has been typeset from a TEX/LATEX file prepared by the author.

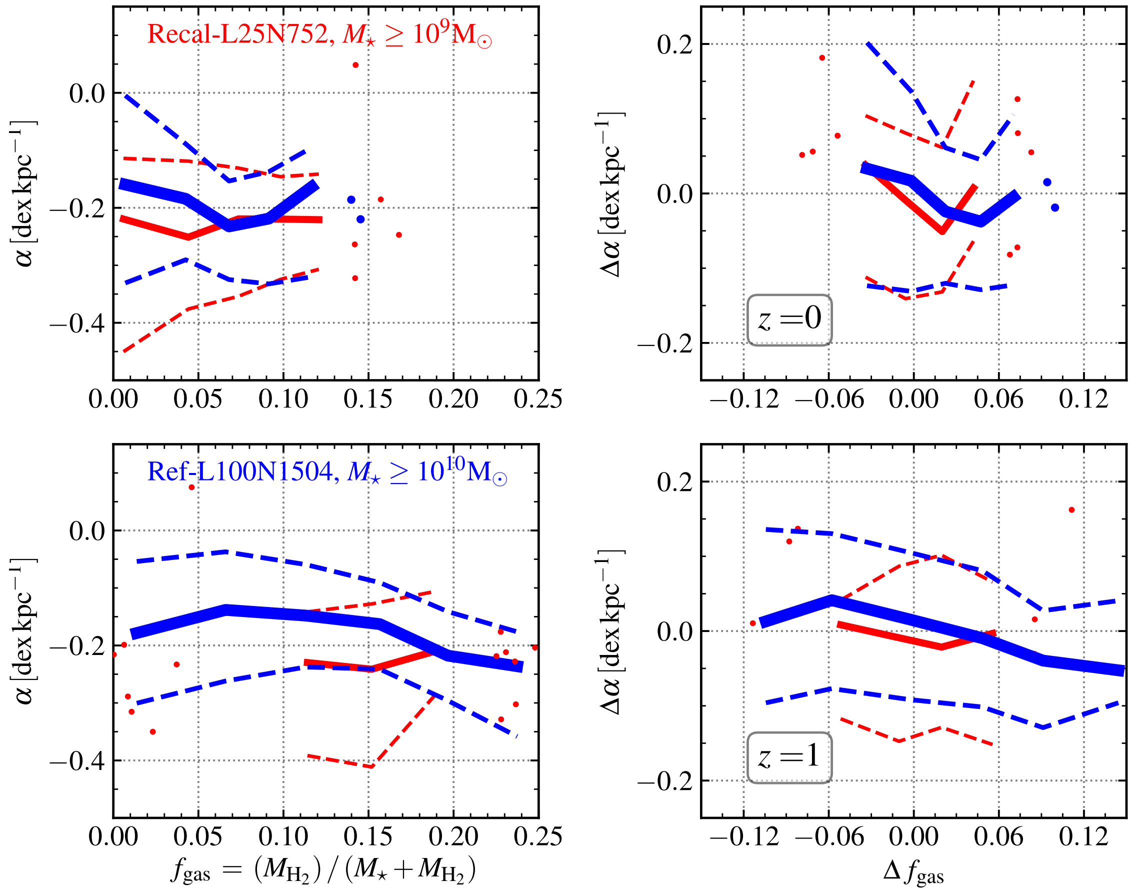

Figure B1. Same as Fig 7, but now taking the contribution of the molecular gas, H_2, in the definition of the gas fraction, i.e., $f_{gas} = H_2/(M_\star + H_2)$.